PERGAMON

International Journal of Solids and Structures 37 (2000) 1019–1043

INTERNATIONAL JOURNAL OF SOLIDS and STRUCTURES

www.elsevier.com/locate/ijsolstr

Analysis of elastically coupled thick-walled composite blades

Ori Rappel, Omri Rand*

Faculty of Aerospace Engineering, Technion–Israel Institute of Technology, Haifa 32000, Israel

Received 4 January 1998; in revised form 21 March 1999

Abstract

A formulation for thick-walled composite blades is devised and implemented numerically. A parametric study which is focused on the influence of wall thickness on the structural behavior of blades, with an emphasize on the elastic couplings induced by composite materials is also presented. In contrast with models for thin-walled blades, the shear stresses perpendicular to the local wall direction are accounted for. The numerical solution is based on a finite-difference scheme where the displacement field is described by four global displacements for each cross-section and an out-of-plane warping function for each material point. Overall, the solution procedure employs an iterative scheme that enables the inclusion of a large number of independent variables. The results reveal and demonstrate the discrepancies between thick-walled modeling and thin-walled modeling as functions of the wall thickness for various loading modes, and supply a clear indication of regions where employing a thick-walled model is inevitable.

1. Introduction

The design of helicopter blades is known to be a compromise between many different and contradicting demands. The different requirements emerge from the vast range of operation conditions, and it is clear that conventional design practice using isotropic materials is not capable of properly fulfilling all requirements. This is partly due to the fact that the structural-dynamics characteristics of isotropic blades do not include enough design degrees of freedom.

The introduction of composite materials to the design of the rotor blades has provided many additional design parameters and degrees of freedom, and one of the promising structural features of composite structures is the ability to introduce passive couplings into the main rotor structure. Being slender structures, rotor blades are viewed and treated as beams, where usage of composite materials

* Corresponding author. Tel.: +972-4-829-3487; Fax: +972-4-823-1848.
E-mail address: aeromri@ae560.technion.ac.il (O. Rand)

0020-7683/00/$ - see front matter
PII: S0020-7683(99)00109-2

may induce couplings between the main elastic deformation components, namely: the transverse displacements, the axial displacement, and the twist. Representative relevant studies of the phenomena associated with the structural modeling of composite blades are: Stemple and Lee, 1989; Chandra et al., 1990; Rapp, 1990; Kim and Dugundji, 1991; Librescu and Song, 1991; Chandra and Chopra, 1991; Yuan et al., 1992; Song and Librescu, 1992; Chandra and Chopra, 1992a, 1992b; Kalfon and Rand, 1993; Bauchau and Chiang, 1993; Venkatesan et al., 1993; Kim and Dugundji, 1993; Straub et al., 1994; Pai and Nayfeh, 1994; Armanios and Badir, 1995; Rand and Barkai, 1996; Epps and Chandra, 1996; Kosmatka and Lake, 1996 and McCarthy and Chattopadhyay, 1996.

The above mentioned references contain many models that are capable of predicting the coupled structural behavior of composite beams. However, only few of these models are capable of handling blades of thick-walled cross-sections (e.g. Pai and Nayfeh, 1994; McCarthy and Chattopadhyay, 1996), and the literature contains no study of the wall thickness influence on the structural behavior of composite beams, and in particular on the associated coupling magnitudes. Likewise, no indication regarding the limitations of thin-walled models in predicting the structural behavior of thick-walled blades is available. On the other hand, part of the current helicopter blades feature very thick walls.

It should be emphasized that unlike the isotropic case, the extension of the prediction capability of solid models to the thick-walled case is not confined to the introduction of additional boundary conditions. This is due to the fact that blades are typically constructed out of the orthotropic laminae which are placed parallel to the local wall direction, and thus, the material system of coordinates varies along the cross-sectional circumference, which complicates the formulation as will be clarified later on. In addition, in contrast with the case of thin-walled beams, the modeling of sharp corners (like the four corners in a box-beam cross-section) is important and poses some modeling difficulties. Thus, the analysis presented in this paper includes the warping and the stress distributions over the wall thickness which requires a much more detailed model with a relatively large number of unknowns.

Since models for thin-walled beams are simpler and more efficient than models that are capable of consistently dealing with thick-walled beams, additional goal of the present study is to explore the limits of applicability of thin-walled models when thick-walled cross-sections are under discussion. Hence, following the model presentation, a parametric study will be presented. The purpose of this study is to supply a quantitative indication regarding the error which is induced by using thin-walled models for increasing values of the wall thickness. The study includes all aspects of the structural behavior including the coupling effects in symmetric and antisymmetric composite beams.

2. Governing equations for a thick-walled composite beam

An illustrative composite box-beam is shown in Fig. 1. Before deformation, the beam is straight, untwisted, and is placed along the X axis, while the coordinates Y and Z define the cross-sectional planes.

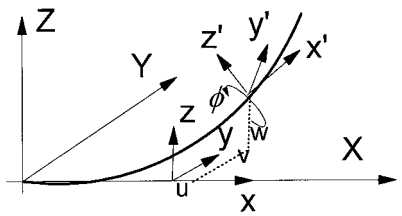

Fig. 1. A general view of a deformed thick-walled blade.

As shown in Fig. 1, and since the beam is a slender structure, the deformation is based on the cross-sectional displacements $u(X)$, $v(X)$, and $w(X)$ in the X, Y, and Z directions, respectively, and a twist angle, $\phi(X)$. These components of the deformation are functions of X only and, therefore, they represent 'rigid' deformation of each cross-section that contains no warping.

To account for the out-of-plane warping, a three-dimensional warping function is superimposed (in the axial direction) upon the above mentioned displacements. This warping function is denoted by Ψ, and is assumed to be of zero average value over the cross-sectional area (i.e. $\iint \Psi \, dA = 0$). Ψ is a function of X, Y, and Z.

A local system of coordinates x–y–z which before deformation is parallel to the X–Y–Z system is located at each cross-section (see Fig. 1). An additional system of coordinates, x'–y'–z', which represents the deformed attitude of the x–y–z system is also defined. According to Kalfon and Rand (1993), one may write:

$$\begin{Bmatrix} x \\ y \\ z \end{Bmatrix} = [D] \begin{Bmatrix} x' \\ y' \\ z' \end{Bmatrix}, \tag{1}$$

where the linear version of $[D]$ which depends on the local deformation is given in Appendix A.

A fourth material system of coordinates ξ–η–ζ which is attached to the contour so that ξ is parallel to the x direction and η is tangent to the local contour is shown in Fig. 2. The angles α_i are measured between the y and the η directions, and r_i is the normal distance to the tangent to the contour at the point under discussion. Hence, α_i and r_i are constants over each segment. The directions ξ–η–ζ are given by:

$$\begin{Bmatrix} \xi \\ \eta \\ \zeta \end{Bmatrix} = \begin{bmatrix} 1 & 0 & 0 \\ 0 & \cos\alpha_i & \sin\alpha_i \\ 0 & -\sin\alpha_i & \cos\alpha_i \end{bmatrix} \begin{Bmatrix} x \\ y \\ z \end{Bmatrix}. \tag{2}$$

The deformation is defined using the radius vectors before and after deformation. This enables the determination of the the tangent base vectors, with the aid of which the Green strain components will be expressed. Before deformation, the radius vector for each material point may be generally expressed as:

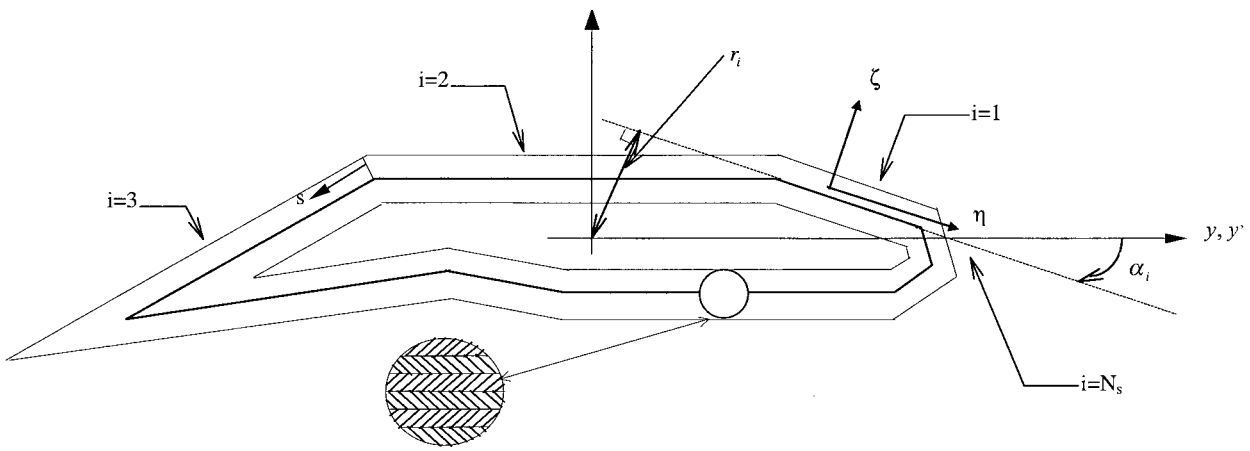

Fig. 2. Discretization of a thick-walled cross-section into N_s straight segments and the contour system of coordinates ξ–η–ζ.

$$\vec{r}_P = X\hat{X} + Y\hat{Y} + Z\hat{Z}, \tag{3}$$

while, after deformation:

$$\vec{R}_P = R_x\hat{X} + R_y\hat{Y} + R_z\hat{Z}, \tag{4}$$

where:

$$\begin{Bmatrix} R_x \\ R_y \\ R_z \end{Bmatrix} = \begin{Bmatrix} X + u(X) \\ v(X) \\ w(X) \end{Bmatrix} + [D] \begin{Bmatrix} \Psi(X,y,z) \\ y \\ z \end{Bmatrix}. \tag{5}$$

The base vectors before and after deformation take the form:

$$\vec{g}_i = \frac{\partial \vec{r}_P}{\partial X_i}, \tag{6a}$$

$$\vec{G}_i = \frac{\partial \vec{R}_P}{\partial X_i},\ X_i = X,Y,Z. \tag{6b}$$

and the resulting strain components are finally determined as:

$$\varepsilon_{ij} = \frac{1}{2}\left[\vec{G}_i\vec{G}_j - \vec{g}_i\vec{g}_j\right]. \tag{7}$$

Since the linear formulation requires no distinction between the deformed and undeformed directions, the above assumed deformation components may be directly used to construct the strain expressions. Considering this linear case, the only nonvanishing strain components are given by:

$$\varepsilon_{xx} = u_{,x} - yv_{,xx} - zw_{,xx} + \Psi_{,x}, \tag{8a}$$

$$\gamma_{xz} = y\phi_{,x} + \Psi_{,z}, \tag{8b}$$

$$\gamma_{xy} = -z\phi_{,x} + \Psi_{,y}, \tag{8c}$$

where ε_{xx} is the normal strain, and γ_{xz}, γ_{xy} are the shear strains and $(\,)_{,x}$ denotes differentiation with respect to x.

Referring to Fig. 3, the above strain components may be described in the material system of coordinates using r (the normal distance to the tangent to the contour at the point under discussion), and n (the distance from the origin of the ξ–η–ζ system to the crossing point of the η axis and the normal distance r). It may be shown that r and n are given by:

$$r = z\cos\alpha - y\sin\alpha, \tag{9a}$$

$$n = y\cos\alpha + z\sin\alpha. \tag{9b}$$

Consequently, the strain components in the ξ–η–ζ system directions are given by:

$$\varepsilon_{\xi\xi} = u_{,\xi} - yv_{,\xi\xi} - zw_{,\xi\xi} + \Psi_{,\xi}, \tag{10a}$$

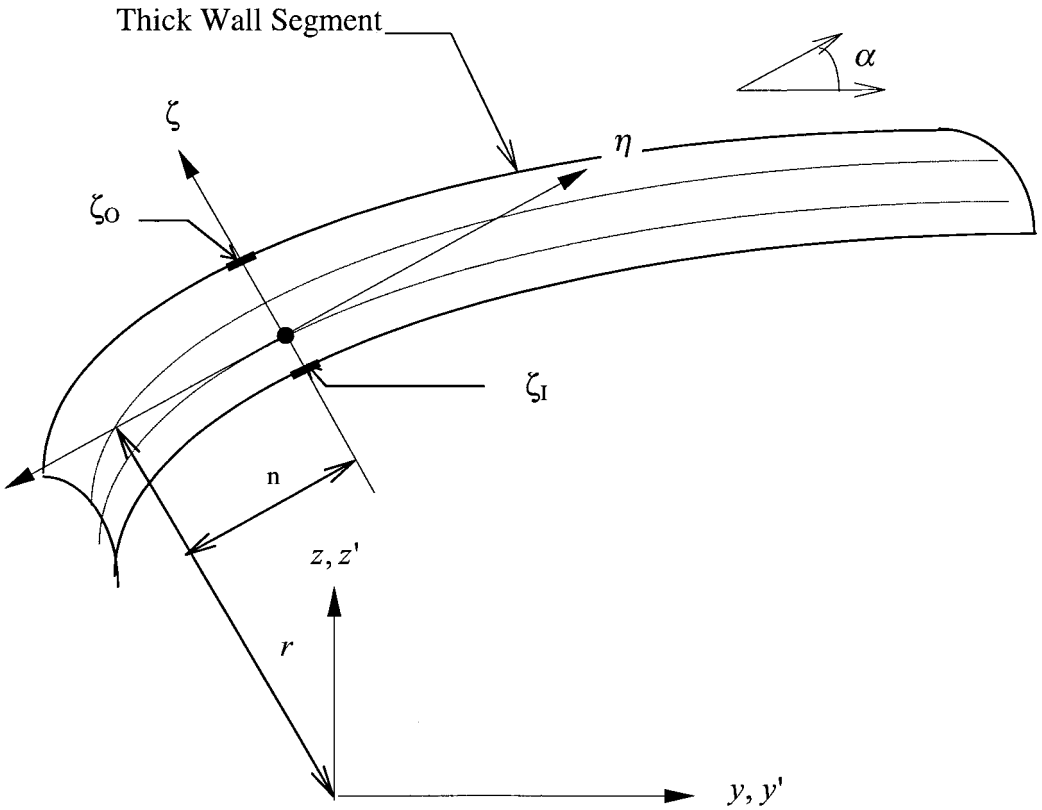

Fig. 3. Definition of the distances r and n.

$$\gamma_{\xi\eta} = \Psi_{,\eta} - r\phi_{,x}, \tag{10b}$$

$$\gamma_{\xi\zeta} = \Psi_{,\zeta} + n\phi_{,x}. \tag{10c}$$

The constitutive relations for a general orthotropic lamina consists of nine independent elastic moduli, C_{ij}, which are functions of the material properties and the local ply angle relative to the x (or ξ) axis (see, e.g. Ochoa and Reddy, 1992). Reduction of these relations for the present case is obtained by exploiting the beam slenderness and assuming $\sigma_{\zeta\zeta} = \tau_{\eta\zeta} = 0$. In addition, the stress $\sigma_{\eta\eta}$ is assumed to vanish due to the neglect of the in-plane warping (i.e. the cross-sectional shape remains 'rigid' in its own plane). Note that the strains $\varepsilon_{\zeta\zeta}$, $\varepsilon_{\eta\eta}$ are not zero (and may be determined based on the values of the strain components $\varepsilon_{\xi\xi}$, and $\gamma_{\xi\zeta}$), and thus, Poisson's ratio effects are included in the above present formulation. Elimination of these assumptions requires the inclusion of the in-plane warping or treating the beam structure as a three-dimensional structure which are beyond the scope of the present model. Thus, by substituting the above assumptions in the general constitutive relations for orthotropic materials, the following reduced relations are obtained:

$$\begin{pmatrix} \sigma_{\xi\xi} \\ \tau_{\xi\zeta} \\ \tau_{\xi\eta} \end{pmatrix} = \begin{bmatrix} C_{11} & 0 & C_{16} \\ 0 & C_{55} & 0 \\ C_{16} & 0 & C_{66} \end{bmatrix} \begin{pmatrix} \varepsilon_{\xi\xi} \\ \gamma_{\xi\zeta} \\ \gamma_{\xi\eta} \end{pmatrix}. \tag{11}$$

The stress resultant over the cross-sectional area may be expressed as:

$$\vec{t} = \sqrt{\vec{g}_x \vec{g}_x}\left(\sigma_{xx}\vec{G}_x + \tau_{xy}\vec{G}_y + \tau_{xz}\vec{G}_z\right), \tag{12}$$

where:

$$\sigma_{xx} = \sigma_{\xi\xi}, \tag{13a}$$

$$\tau_{xy} = \tau_{\xi\eta}\cos\alpha - \tau_{\xi\zeta}\sin\alpha, \tag{13b}$$

$$\tau_{xz} = \tau_{\xi\eta}\sin\alpha + \tau_{\xi\zeta}\cos\alpha. \tag{13c}$$

As indicated above, the deformation is defined using four cross-sectional displacement components (u, v, w and ϕ) and a local warping function (Ψ). Likewise, equilibrium is achieved by four integral equations and one differential equation. The integral equations equate the cross-sectional resultants F_x (in the x direction), F_y (in the y direction), F_z (in the z direction) and the moment resultant M_x (in the x direction) that are induced by the external resultant loads to the corresponding loads obtained by stress integrations, namely:

$$F_x = \int\int_A \sigma_{\xi\xi}\,\mathrm{d}A, \tag{14a}$$

$$F_y = \int\int_A (\tau_{\xi\eta}\cos\alpha - \tau_{\xi\zeta}\sin\alpha)\mathrm{d}A, \tag{14b}$$

$$F_z = \int\int_A (\tau_{\xi\eta}\sin\alpha + \tau_{\xi\zeta}\cos\alpha)\mathrm{d}A, \tag{14c}$$

$$M_x = \int\int_A (n\tau_{\xi\zeta} - r\tau_{\xi\eta})\mathrm{d}A. \tag{14d}$$

The differential equation of equilibrium is the associated differential equilibrium equation in the x (or ξ) direction which is given by:

$$\sigma_{\xi\xi,\xi} - \tau_{\xi\eta,\eta} + \tau_{\xi\zeta,\zeta} + B_\xi = 0, \tag{15}$$

where B_ξ is the body force in the x direction. To assure consistency of the above integral and differential equations in the x direction, one should require $F_{x,x} = -\int\int B_\xi\,\mathrm{d}A$.

There are eight beam-type boundary conditions at the beam root and tip. For a clamped-free beam, six of them are the following geometrical boundary conditions at the beam root:

$$u = v = v_{,x} = w = w_{,x} = \phi = 0. \tag{16}$$

The remaining two natural boundary conditions at the beam tip are based on equating the external transverse tip moments, M_y^{tip} and M_z^{tip}, to those obtained by stress integrations over the tip cross-sectional area, A^t, namely:

$$\left(M_y^t, M_z^t\right) = \int\int_{A^t} (\sigma_{\xi\xi}z, -\sigma_{\xi\xi}y)\mathrm{d}A^t. \tag{17}$$

Additional contour boundary condition that ensures traction-free surface along the beam should be taken into account. This condition may be expressed as (see Fig. 3):

$$\tau_{\xi\zeta} = 0 \text{ for } \zeta = \zeta_I, \zeta_O. \tag{18}$$

As shown, the above formulation consistently includes body forces in the x direction and, therefore, may adequately be used to predict also the effect of rotation on the behavior of composite blades.

3. The numerical methodology

3.1. The discretization

Based on the above linear formulation, a finite-difference numerical scheme that may handle general geometries and lamination modes of thick-walled cross-sections has been derived. Within this approach, each straight segment is divided into small cells as shown in Fig. 4(a) for a rectangular cross-section (detailed notation is provided for the upper flange only which is numbered $i = 1$). As shown, the cells along the thickness direction are numbered by the index l ($=1,2,\ldots, L$) and the cells along the wall direction by the index n ($=1,2,\ldots, N_i$). Similar discretization is applied to all segments. Subsequently a value of $\Psi^i(n,l)$ ($i = 1,2,\ldots, N_s$) is assigned for the out-of-plane warping function at the middle point of each cell.

In contrast with thin-walled cross-sections, the discretization of a thick-walled cross-section poses some difficulties. On one hand, it is clear that the orthotropic material laminae are placed parallel to the wall direction. On the other hand, and as already mentioned, it is not clear what is the exact way in which segments are connected in 'real' thick-walled cross-sections, and therefore, the modeling of the connecting points between segments is questionable. The technique adopted in the present analysis is based on the definition of an overlapping factor, C_A, that determines the amount of overlapping area between adjoint segments. It is expected that $0 < C_A < 1$ will supply a realistic corner modeling in this case. The sensitivity of the results to C_A will be discussed later on.

3.2. The system of equations

With the aid of Eqs. (14a), (14b), (14c), (14d) and (5), it is possible to express the equilibrium equations in terms of the displacements and to construct a linear system of $(N \times L \times N_s)+4$ equations and unknowns that may be written as:

$$[S]\{U\} = \{f\}, \tag{19}$$

where the unknown vector, $\{U\}$, is given by

$$\{U\} = \langle u_{,x}, v_{,xxx}, w_{,xxx}, \phi_{,x}, \Psi^1(1,1), \ldots, \Psi^{N_s}(N,L)\rangle^T. \tag{20}$$

The local differential equation Eq. (15) supplies one equation per each cell while the integral equilibrium equations (Eqs. (14a), (14b), (14c) and (14d)) supply the additional four integral equations. Consequently, the loading vector $\{f\}$ consists of the external resultant loads and all other quantities that do not contain components of $\{U\}$. Generally, this vector may be written as:

$$\{f\}^T = \left\{f_1, f_2, f_3, f_4, f^1, f^2, f^3, \ldots, f^M\right\}, \tag{21}$$

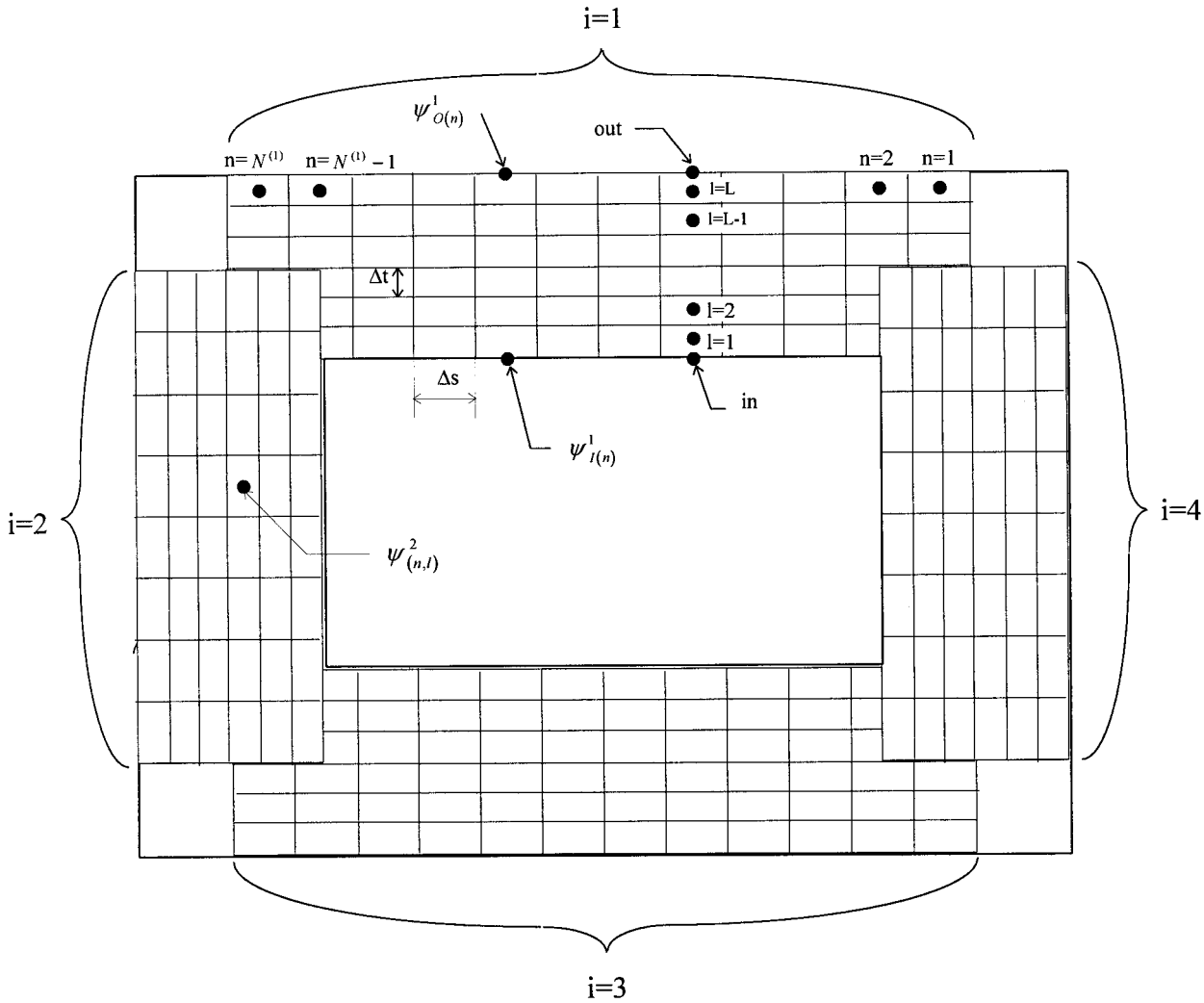

Fig. 4. Discretization of a thick-walled box-beam into $N_s = 4$ segments, and a discretization of each segment into N segments along its length and L segments along its thickness.

where:

$$f_1 = F_x + f_x\left(v_{,xx}, w_{,xx}, \Psi^i(n,l)_{,x}\right), \tag{22a}$$

$$f_2 = F_y + f_y\left(v_{,xx}, w_{,xx}, \Psi^i(n,l)_{,x}\right), \tag{22b}$$

$$f_3 = F_z, \tag{22c}$$

$$f_4 = M_x + m_x\left(v_{,xx}, w_{,xx}, \Psi^i(n,l)_{,x}\right) \tag{22d}$$

$$f^{\,i} = f^{\,i}\left(u_{,xx}, v_{,xx}, w_{,xx}, \Psi^i(n,l)_{,x}, \Psi^i(n,l)_{,xx}, \Psi^i(n,l)_{,xy}, \phi_{,xx}, B_\xi\right). \tag{22e}$$

Note that all the terms of the matrix $[S]$ and the functions f_x, f_y, m_x and f^i are also explicit functions of the cross-sectional geometry and the lamination mode. All derivatives with respect to y, z or s are expressed using a finite-difference scheme.

As shown, most of the computational effort is invested in the warping modeling. The above formulation includes $N \times L \times N_s$ warping unknowns and only 4 cross-sectional displacements. This demonstrates the basic difference between isotropic and composite beam analysis (note that in the isotropic case, the warping and the shear modeling are not essential for the determination of the axial stresses).

3.3. The contour boundary conditions

For a thick-walled cross-section, the contour boundary condition (18) may also be expressed by a finite-difference scheme. This results in additional $2 \times N \times N_s$ equations (one per each boundary segment), and the same number of additional unknowns which are the warping values at the segment boundary edges, $\Psi^i_I(n)$ and $\Psi^i_O(n)$, see Fig. 4(a).

The contour boundary condition may be described as $\tau_{\xi\zeta} = 0$, or $C_{55}(\psi_{,\zeta} + n\phi_{,x}) = 0$, which may be expressed as:

$$\Psi_{,\zeta} = -n\phi_{,x}. \tag{23}$$

To implement the above condition, Ψ is expressed using a polynomial expansion in the ζ direction at the contour vicinities. To demonstrate that for the inner contour at the cell column n over segment i = 1 [see Fig. 4(a)], Ψ is expressed as:

$$\Psi = a_0 + a_1\zeta + a_2\zeta^2. \tag{24}$$

By substituting the first three points values $\Psi^1_I(n)$, $\Psi^{\,1}(n,1)$, $\Psi^{\,1}(n,2)$ and the corresponding ζ values, ζ_0, $\zeta_0 + \Delta t/2$ and $\zeta_0 + 3\Delta t/2$, respectively, in Eq. (24) (where ζ_0 is the ζ coordinate of the inner boundary), it is possible to express a_0, a_1 and a_2 in terms of $\Psi^1_I(n)$, $\Psi^{\,1}(n,1)$, $\Psi^{\,1}(n,2)$ and Δt, and the corresponding boundary equation becomes $a_1 + 2a_2\zeta_0 = -n\phi_{,x}$ ($= \Psi_{,\zeta}$ at $\zeta = \zeta_0$).

More details about this procedure and expressions for the components of the matrix $[S]$ may be found in Rappel, 1997.

3.4. The iterative scheme

The iterative scheme is initiated by some deformation assumption. Then, the resultant external loads at discrete cross-sections along the beam are evaluated. Subsequently, Eq. (19) is solved and the unknown vector, $\{U\}$, is obtained for each cross-section. The natural boundary conditions at the beam tip (Eq. (17)) are then used to obtain the values of $v_{,xx}, w_{,xx}$ there. This is done by expressing the stress components of Eq. (17) in terms of the displacements which yields two equations where the only unknowns are $v_{,xx}$ and $w_{,xx}$. These values are then integrated along the beam and the distributions of $v_{,xx}(x)$ and $w_{,xx}(x)$ are obtained. With the aid of the geometric boundary conditions at the root (Eq. (16)), the distributions of u, $v_{,x}$, $w_{,x}$, v, w and ϕ along the beam are also determined. Using this new estimation of the deformation, the vector $\{f\}$ at each cross-section is updated (since it is a function of

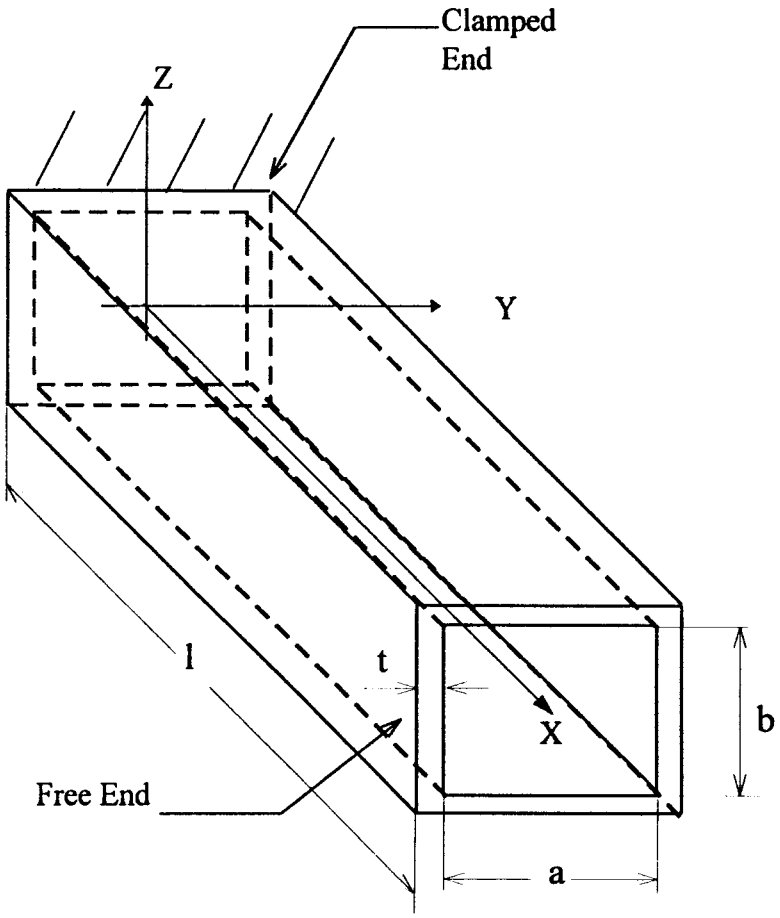

Fig. 5. Thick-walled box-beam notation.

longitudinal derivatives of the unknowns (see Eqs. (22a), (22b), (22c), (22d) and (22e)) and the iterative process is repeated until convergence is achieved. Numerical study has shown that the above quasi-linear scheme exhibits reasonable convergence characteristics.

4. Results

To demonstrate the capabilities and some numerical aspects of the present formulation and solution procedure, the study presented in this section has been carried out for the composite box-beam shown in Fig. 5. As shown, the beam length, width, height and thickness are denoted l, a, b and t, respectively, and the results presented in this paper are for typical Graphite/Epoxy laminae with the following material properties: $E_{11} = 142. \times 10^9$ N/m^2, $E_{22} = E_{33} = 9.8 \times 10^9$ N/m^2, $G_{12} = G_{13} = 6.0 \times 10^9$ N/m2, $G_{23} = 4.8 \times 10^9$ N/m^2, $\nu_{12} = \nu_{13} = 0.42$, $\nu_{23} = 0.5$.

Part of the following discussion makes use of results obtained for thin-walled models. Such results were acquired by using the present model with a single cell along its thickness, namely $L = 1$ [see Fig. 4(a)], and ignoring the boundary conditions of Eq. (18).

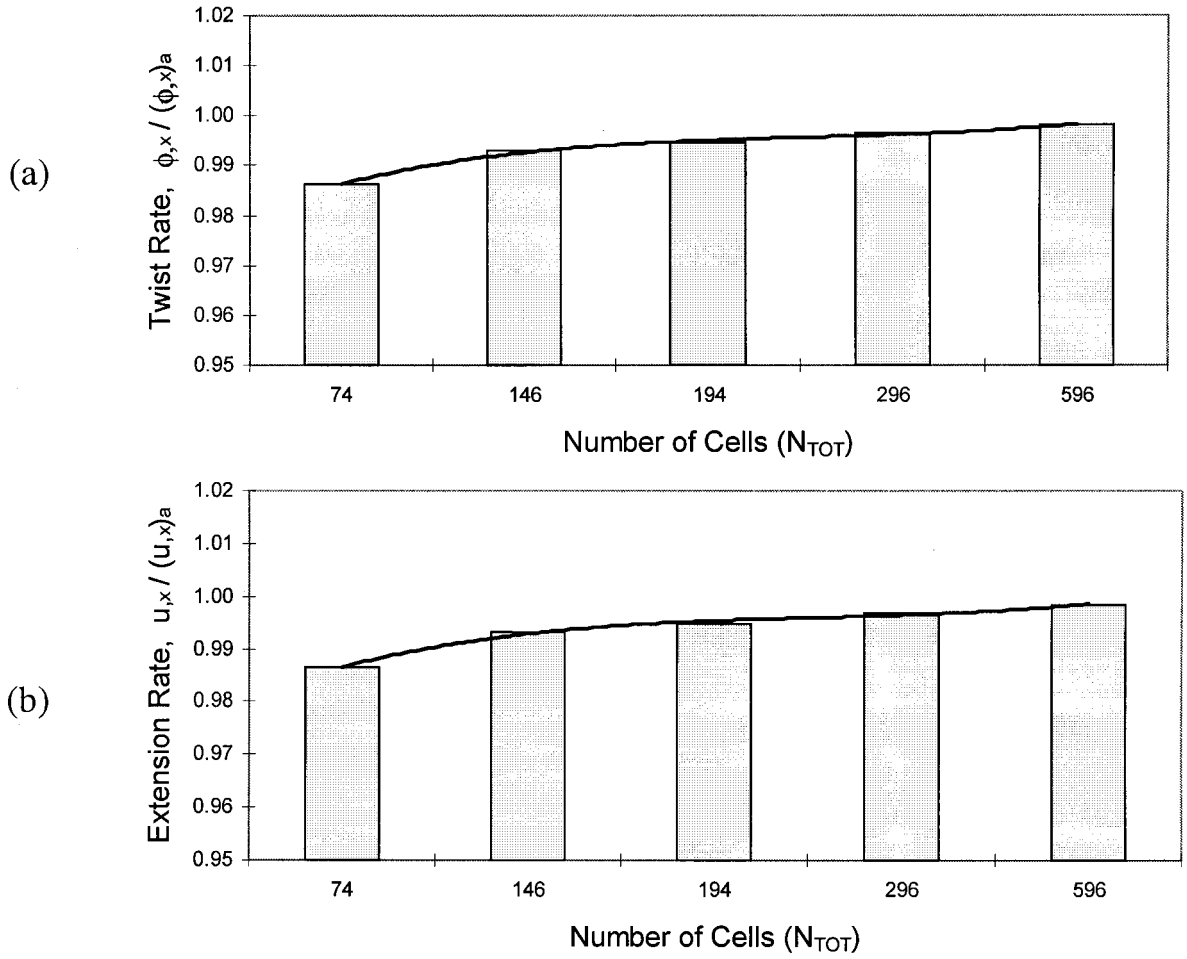

Fig. 6. Sensitivity of an antisymmetric thin-walled Graphite–Epoxy box-beam under tip moment to the number of circumferential cells, N_{TOT} (uniform lamination angle of 15°, $a = 0.039$ m, $b = 0.019$ m, $t = 0.001$ m, $M^{tip} = 1$ N·m): (a) The twist rate (the analytic value is $(\phi_{,x})_a = 8.66 \times 10^{-4}$ rad/m, (b) The extension rate (the analytic value is $(u_{,x})_a = 2.66 \times 10^{-6}$.

4.1. Validation

4.1.1. Discretization refinement

Since the computation effort increases as a cubic function of the number of cells, the required number of cells has been determined first. As an example, a composite antisymmetric thin-walled beam undergoing a torsional moment was studied. Fig. 6(a) shows the beam twist rate due to a tip torsional moment as a function of the number of cells along the circumference $N_{TOT} = N^{(1)} + N^{(2)} + N^{(3)} + N^{(4)}$ (note that only one cell in the wall thickness direction is employed for a thin-walled structure). The results are also compared with the analytical expressions of Rand and Barkai (1996). As shown, the results asymptotically approach a constant value which also agrees with the analytical result. The corresponding extension rate described in Fig. 6(b) exhibits similarly. Based on these results, and on additional similar results obtained for other loading modes, a number of $N_{TOT} = 150$ cells along the circumference has been chosen for the correlations described in what follows. Similar study has shown

that for walls which are uniformly laminated along their thickness, $L = 5$ [see Fig. 4(a)] is sufficient. Since no analytic solution exists in this case, the above study was confined to the convergence of the numerical results only.

4.1.2. Composite beam behavior

Since no published results for the behavior of thick-walled beams are available, the following validation of the numerical model are confined to correlation with thin-walled models.

As a first step, the present model results were correlated with well established results for thin-walled cross-sections. A correlation with experimental and finite-element based theoretical results reported in Chandra et al. (1990) has been carried out. Representative results for antisymmetric box-beam under a tip torsional moment and axial force are presented in Fig. 7(a,b). In both cases, the resulting twist is presented. As shown, the present analysis generates reasonable prediction capability. A vast range of similar correlations has produced an analogous conclusion.

4.2. Thick-walled cross-sections

Various thick-walled rectangular cross-sections are presented in Fig. 8. Subsequently, a thickness coefficient has been defined as $C_t = t/a$. As shown in Fig. 8, a thickness coefficient of about 0.2 represents an upper realistic value of the thick-walled rectangular cross-section. Beyond that, a three-dimensional treatment seems to be inevitable.

4.2.1. Influence of the overlapping parameter

Fig. 9(a,b) presents the influence of the overlapping parameter, C_A, on the resulting extension rate, twist rate and the bending curvature rate in isotropic thick-walled box-beams. As expected, the sensitivity to C_A is higher for higher C_t values. Overall, an overlapping parameter in the range of $0.55 < C_A < 0.6$ produces reasonable correlation and this value has been chosen for the present study.

4.2.2. Influence of the wall thickness

The influence of the wall thickness in isotropic beams has been studied first. Fig. 10(a) presents the $w_{,xxx}$ values created by a tip load over a thick-walled isotropic beam as a function of the thickness coefficient. The values are normalized by the analytic expression for the thick-walled case. As shown, the value obtained for the thick-walled model is practically unit regardless C_t. However, the thin-walled model produces higher $w_{,xxx}$ values. This is mainly due to the erroneous low estimation of the moment of inertia in this case.

Similarly, the behavior of thick-walled beam undergoing a tip torsional moment is presented in Fig. 10(b). In the absence of a closed-form solution for thick-walled cross-sections for the present loading mode, the reference analytic values are for thin-walled cross-section. Similar to Fig. 10(a), it is shown that for a thick-walled cross-section, the torsional rigidity is increasing as a function of t in a more rapid manner than the one predicted by the thin-walled solution (and therefore $\phi_{,x}$ of the thick-walled beam is lower). Phenomenally, this result is expected, and can be analytically demonstrated in the case of a circular thick-walled cross-section which is bounded by the radii r and R. In this case, the approximate torsional rigidity (which is based on the thin-walled assumptions) is given by $J_a/\pi R^4 = (1+\tilde{r})^3(1-\tilde{r})/4$, where $\tilde{r} = r/R$. However, the exact solution in this case is $J/\pi R^4 = (1+\tilde{r}^4)/2$ and, therefore, $J_a/J = (1+\tilde{r})^2/(1+\tilde{r}^2)/2$. Clearly $J_a/J \to 1$ when $\tilde{r} \to 1$ (i.e. the thin-walled case) and $J_a/J < 1$ for lower values of $\tilde{r}$ (i.e. as the thickness increases). For $\tilde{r} = 0.5$, which corresponds to $C_t = 0.5$, $J_a/J = 0.9$. It is important to note that the characteristics of a rectangular cross-section presented in Fig. 10(b) show considerably larger discrepancies between the approximate and exact rigidity, and thus, it may be

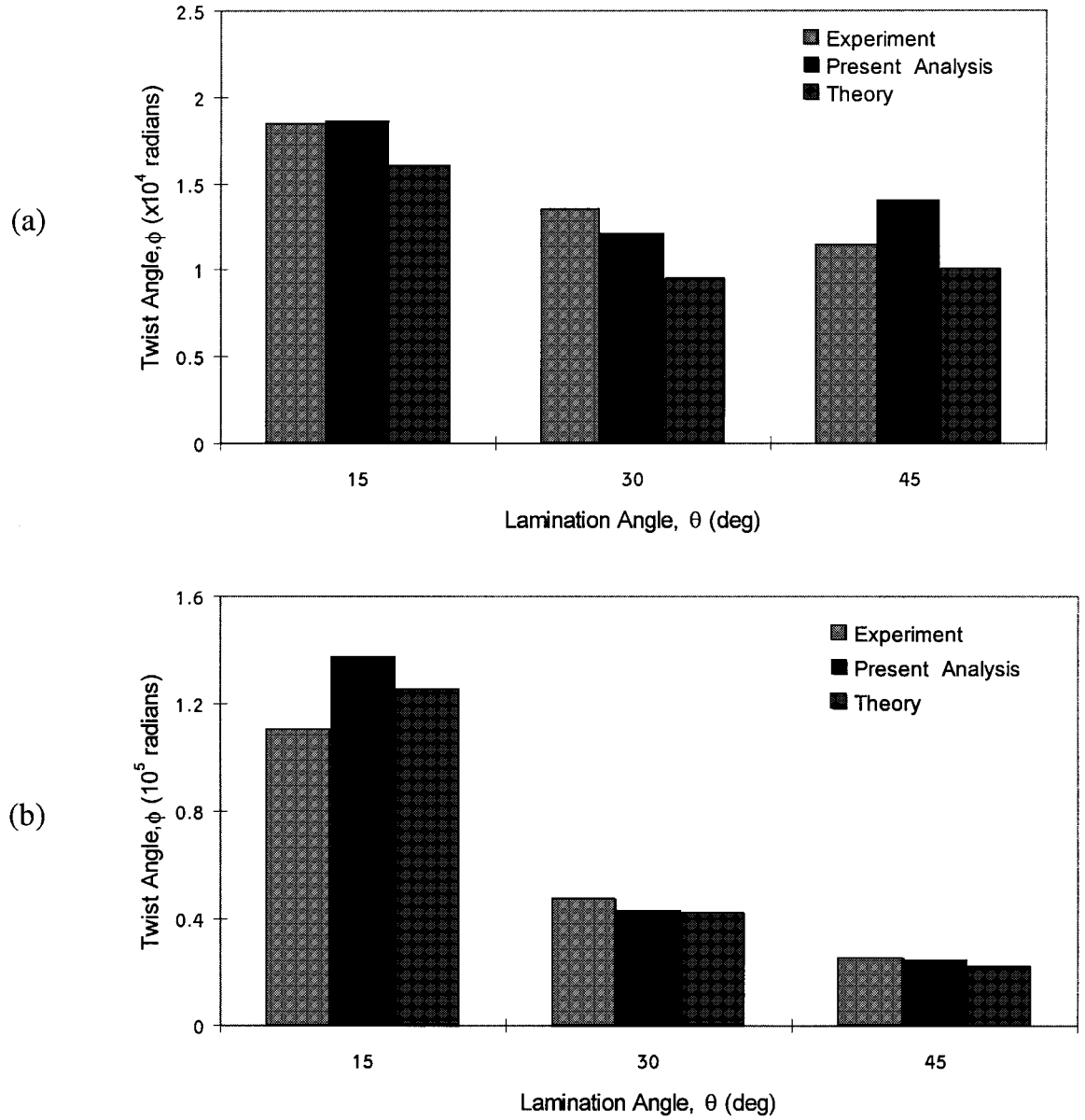

Fig. 7. Correlation of the present analysis results for antisymmetric thin-walled Graphite–Epoxy box-beam with the experimental and Finite-Element theoretical results of Chandra et al. (1990). (a = 0.024 m, b = 0.012 m, t = 0.00076 m): (a) The twist at x/l = 0.5 due to a tip torsional moment of $M^{\text{tip}} = 1$ lb·in, (b) The twist at x/l = 0.5 due to a tip axial force of $F_x^{\text{tip}} = 1$ lb.

concluded that a rectangular cross-section is much more sensitive to the thickness coefficient than a circular cross-section.

4.2.3. Antisymmetric composite beams

Within this section, the discussion will deal with the influence of the wall thickness on the behavior of

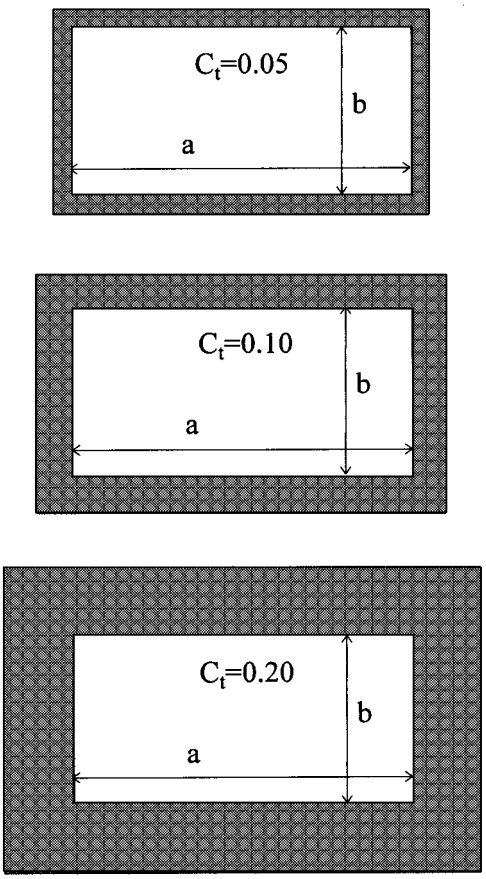

Fig. 8. Definition of the thickness coefficient C_t for a cross-section of $a/b = 2$.

antisymmetric composite beams, and in particular, the influence of the wall thickness on the induced couplings. First, for a loading of a tip torsional moment, Fig. 11(a,b) present the resulting twist and extension rates. All values are normalized with the analytic solution results for this case (see Rand and Barkai, 1996). As shown, for $C_t = 0.25$, $(u,_x)/(u,_x)_a \cong 0.80$ while $(\phi,_x)/(_\phi,_x)_a \cong 0.79$ and, in other words, an error of about 20% in the prediction of both $(u,_x)$ and $(\phi,_x)$ is obtained when a thin-walled model is applied to a thick-walled cross-section of the above thickness coefficient. However, since the functions shown in Fig. 11(a,b) are practically identical, the coupling magnitude $\phi,_x/u,_x$ for this case is not modified by the wall thickness compared with the one predicted using a thin-walled model.

Fig. 12(a,b) shows that when a tip axial force is applied, the resulting values for $C_t = 0.25$ are $(\phi,_x)/(\phi,_x)_a \cong 0.79$ and $(u,_x)/(u,_x)_a \cong 0.90$. Thus, as indicated by Fig. 13, the prediction of the coupling magnitude $\phi,_x/u,_x$ using a thin-walled model induces an error of about 20% for $C_t \cong 0.25$. Note that, as expected, reciprocity (namely, $\phi,_x/F_x^{\text{tip}} = u,_x/M^{\text{tip}}$) is maintained and demonstrated by the fact that Fig. 11(b) and Fig. 12(a) are practically identical.

The reader should note that for the case of axial force, the different axial strain distribution in thick-walled cross-section (compared with thin-walled cross-section) induces different shear stress distribution and subsequently different twist angle. This is due to the 'effective arm' of the induced shear stresses

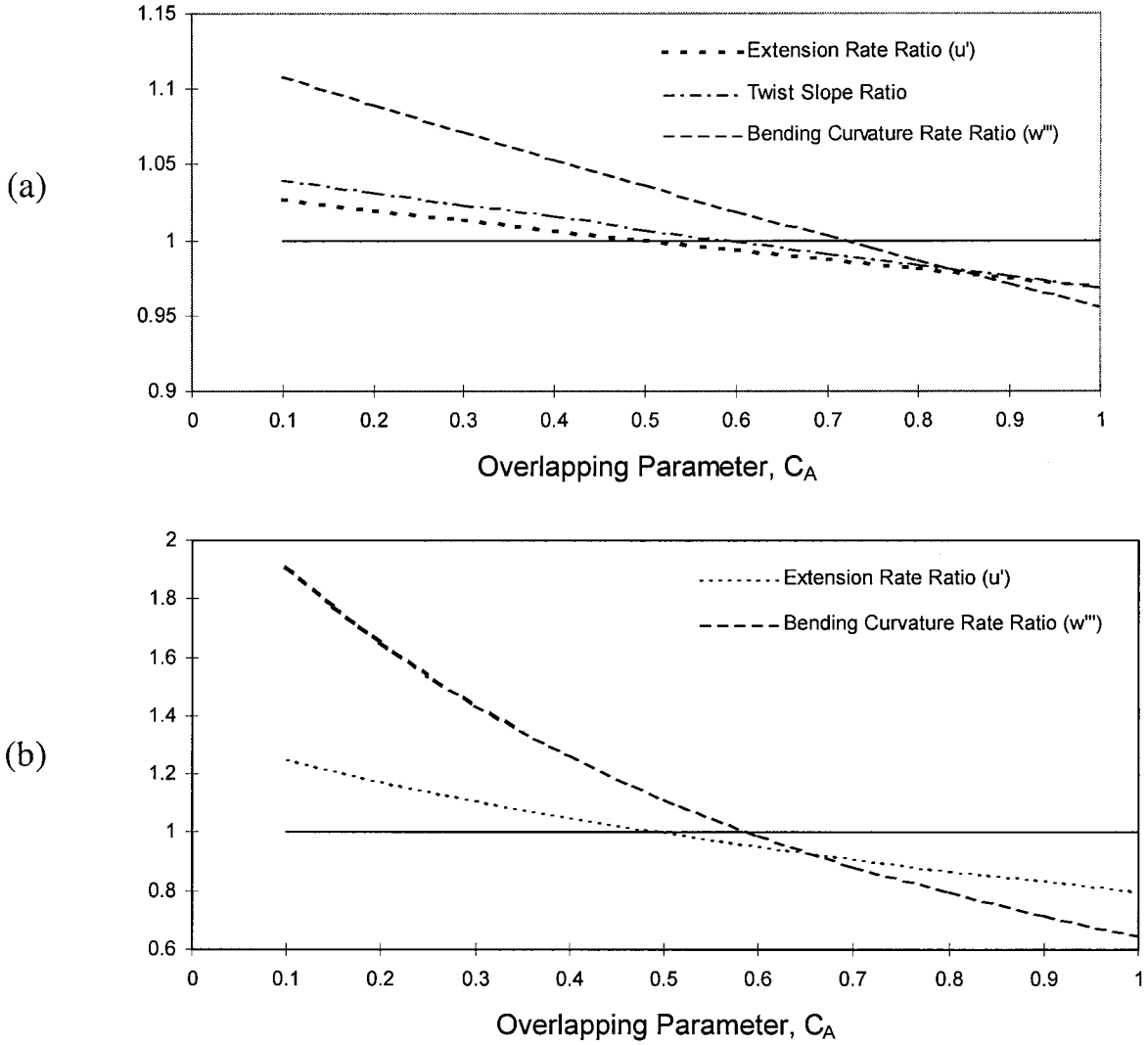

Fig. 9. Isotropic box-beam behavior for various overlapping parameter, C_A (a = 0.024 m, b = 0.012 m, M^{tip} = 1 N·m): (a) C_t = 0.0256, (b): C_t = 0.256.

which is different compared with the one obtained in thin-walled cross-section. However, for the case of torsional moment, the different shear strain distribution in thick-walled cross-section does induce a different distribution of axial stress, however, this distribution does not have a significant influence on the axial resultants.

The out-of-plane warping distribution is also influenced by the wall thickness. The warping distribution along the circumference and the thickness of a cross-section with a C_t = 0.168 is shown in Fig. 14. As shown, the warping over the central line (the 3rd layer of cells) is similar to the case of thin-walled cross-section. Note that the warping vanishes over the flanges and webs middle points. Also, in the vertical segments, the (absolute value of the) warping is higher over the inner boundary, while in the

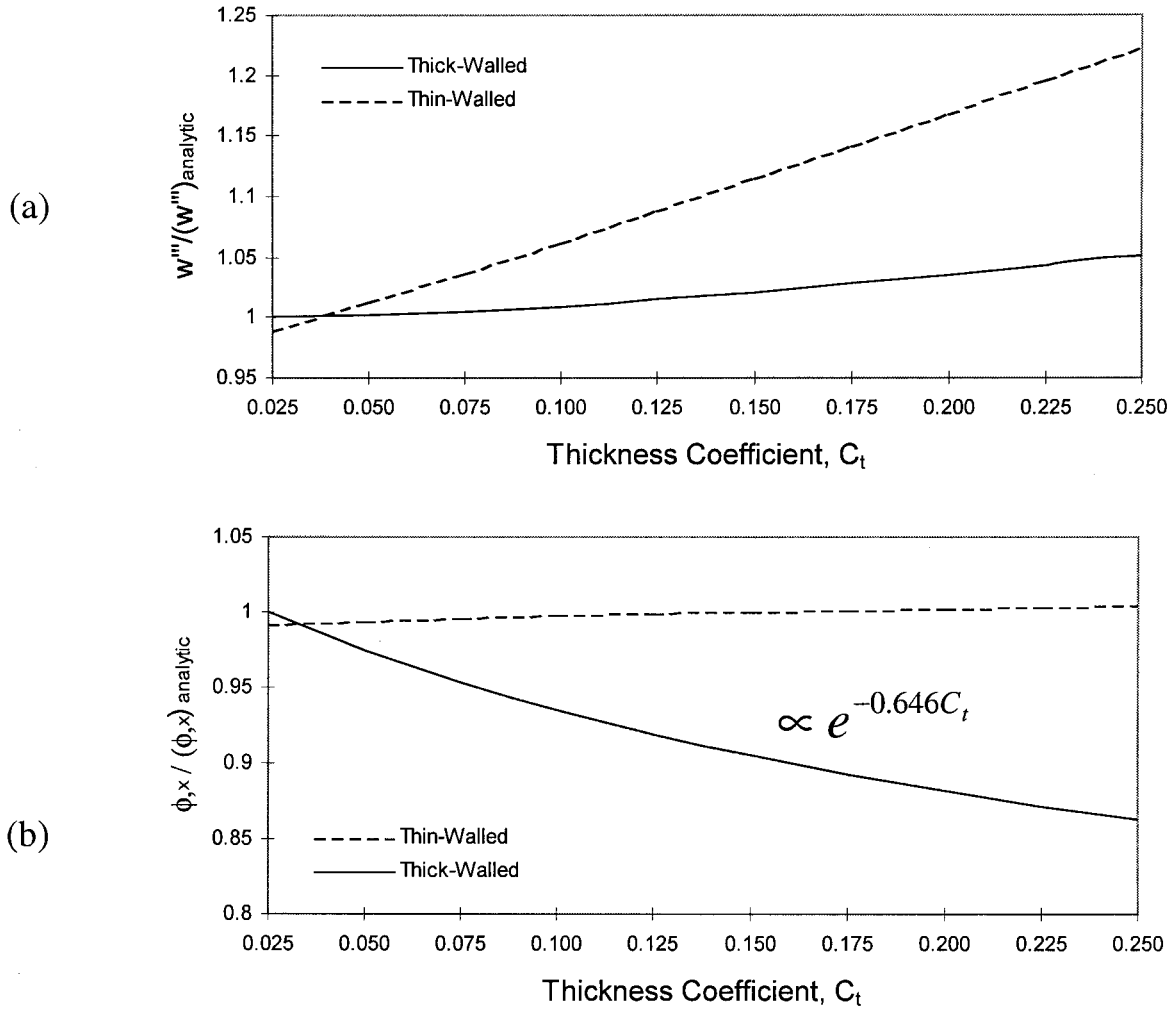

Fig. 10. The values of $w_{,xxx}$ and $\phi_{,x}$ for an isotropic box-beam as predicted by thin-walled and thick-walled models as a function of the thickness coefficient: (a) The bending curvature due to a tip bending force normalized by the corresponding thick-walled analytic solution; (b) The twist due to a tip torsional moment normalized by the corresponding thin-walled analytic solution.

horizontal segments, the warping is higher over the outer boundary. Fig. 15 shows that the warping is a linear function of the thickness, and decreases dramatically as the wall thickness is increased.

The corresponding axial stress is presented in Fig. 16. The fact that the axial stress is almost symmetric about the wall middle plane shows that this stress is mainly a bending stress of the flange. This axial stress dramatically decreases with the wall thickness, and therefore, the cross-sectional tendency to bend is also smaller for a thick cross-section.

The stresses $\tau_{\xi\eta}$ and $\tau_{\xi\zeta}$ are presented in Fig. 17(a,b). As shown, $\tau_{\xi\eta}$ is a linear function of the thickness while $\tau_{\xi\zeta}$ exhibits a 'parabolic' variation over the wall thickness. Note that while $\tau_{\xi\eta}$ decreases with C_t, $\tau_{\xi\zeta}$ increases with C_t (while the analytic solution for thin-walled cross-sections predicts no $\tau_{\xi\zeta}$

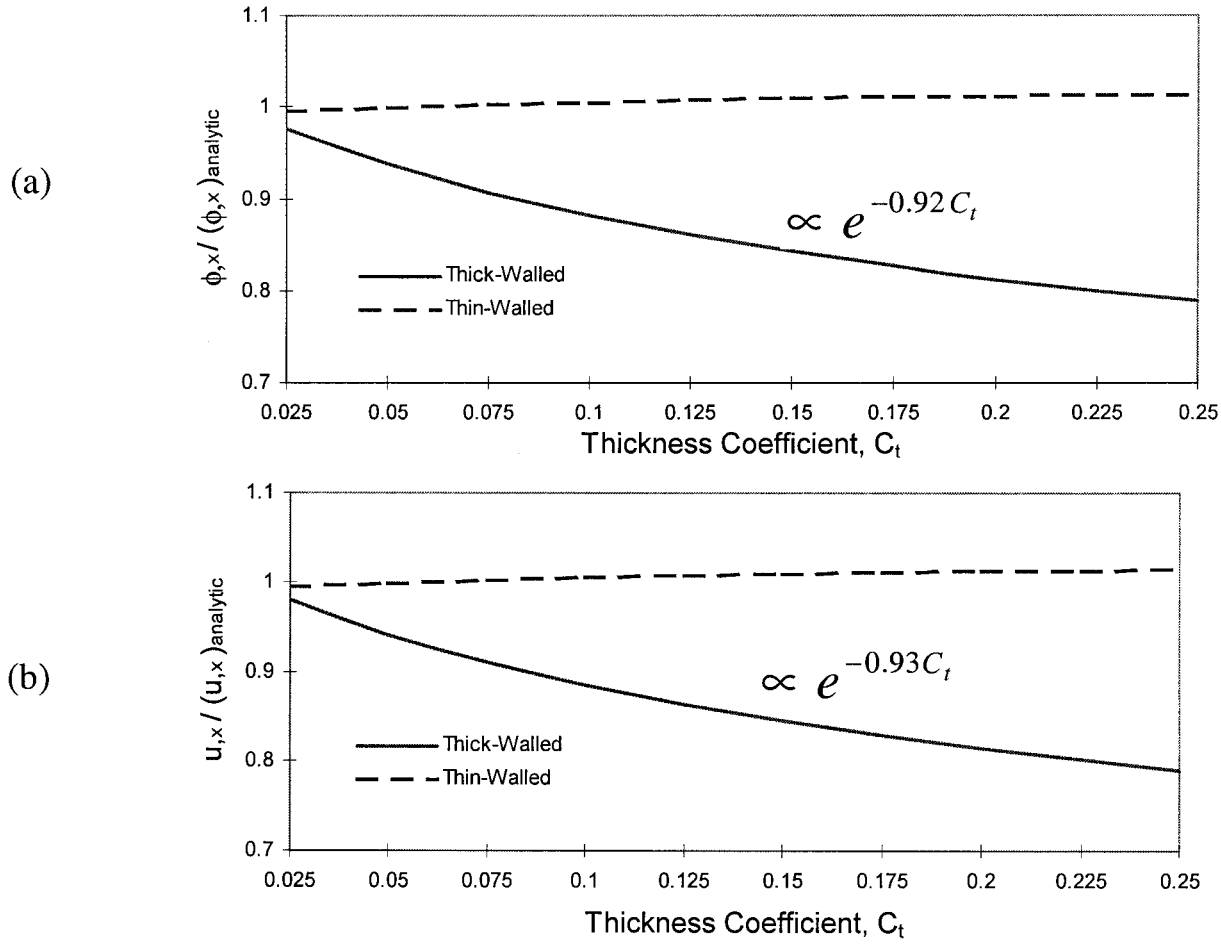

Fig. 11. Antisymmetric composite box-beam response to a tip torsional moment as predicted by thin-walled and thick-walled models normalized by the corresponding thin-walled solution as functions of the thickness coefficient (uniform lamination angle of 15°, $a = 0.024$ m, $b = 0.012$ m, $t = 0.00076$ m, $M_x^{tip} = 1$ N · m): (a) The values of $\phi_{,x}$; (b) The values of $u_{,x}$.

stresses at all). This behavior validates again the classical thin-walled assumptions (namely $\tau_{\xi\eta}(\zeta) \cong \tau_{\xi\eta}(\zeta = 0) = \text{const.}$ and $\tau_{\xi\zeta} = 0$).

4.2.4. Symmetric composite beams

To demonstrate the thickness effect in symmetric beams, a symmetric blade has been constructed out of two flanges with identical unbalanced ply angle of $[\theta]_{10}$ (which therefore features $C_{16} \neq 0$) with a web ply angle of $[\theta,-\theta]_5$ (i.e. $C_{16} = 0$). The cantilever beam has been loaded with a tip beamwise load. It is well known that such a beam exhibits a 'Bending–Torsion' coupling which in the present case induces elastic beamwise bending and twist — see, e.g. Rand (1994, 1998). Thus, the purpose of the present study was to demonstrate the error induced by thin-walled models as a function of the wall thickness. It

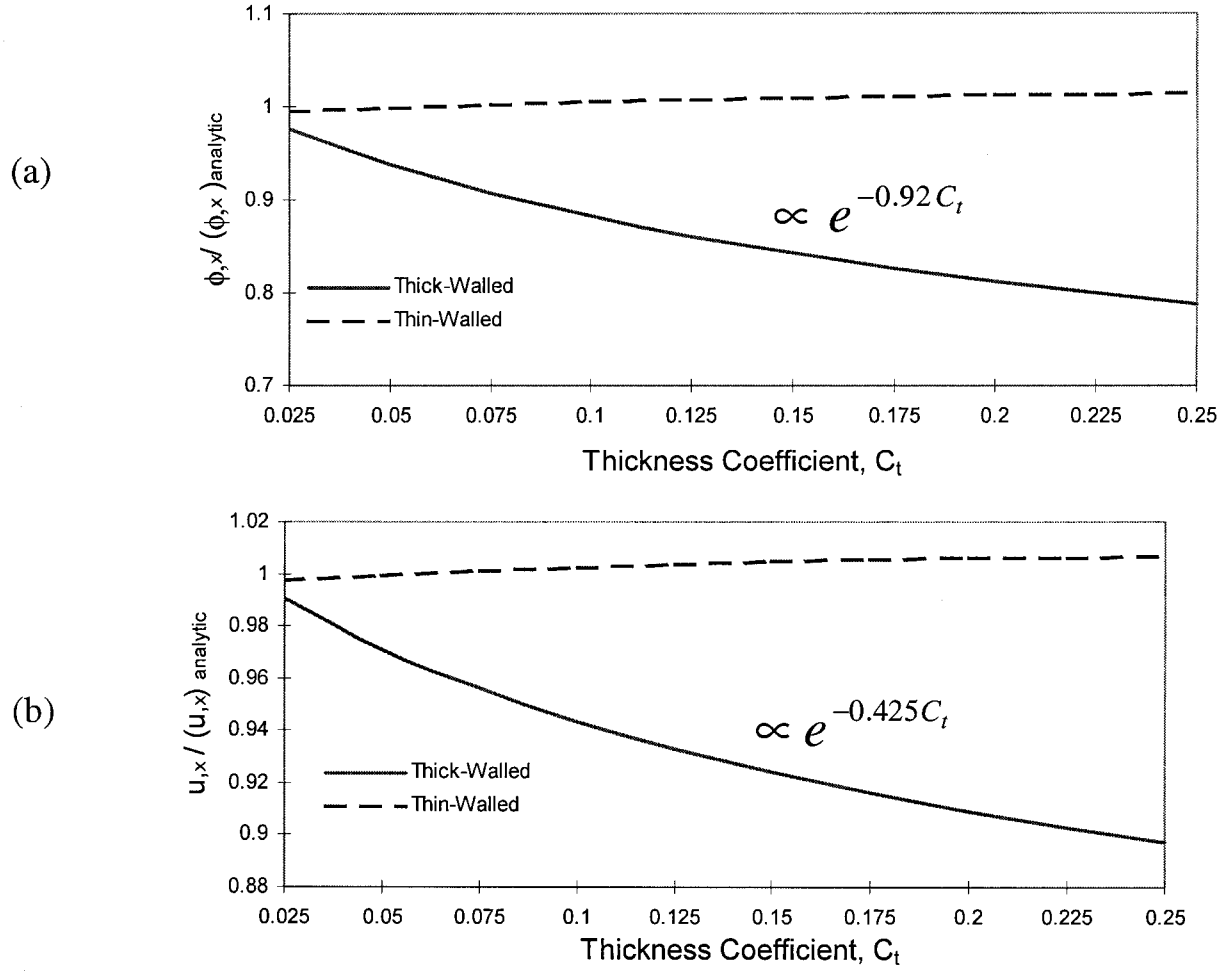

Fig. 12. Antisymmetric composite box-beam response to a tip axial force normalized by the corresponding analytic thin-walled solution as a function of the thickness coefficient (uniform lamination angle of 15°, $a/b = 2$): (a) The values of $\phi_{,x}$; (b) The values of $u_{,x}$.

should be noted that unlike the case of the antisymmetric beam, the twist ($\phi_{,x}$) is not constant along the beam and so the bending curvature ($w_{,xx}$).

Fig. 18 presents the resulting beamwise displacement and twist angle as obtained by the present thick-walled analysis normalized by the corresponding deformation as obtained by a thin-walled analysis for three spanwise locations. The ratio between the results of the above two methods may be approximated by $e^{-3.4C_t}$ for both the beamwise displacement and the twist angle. Only small differences are observed between the various spanwise locations.

Fig. 19 presents the corresponding coupling magnitude. As shown, for $C_t = 0.2$ an error of about 8–10% is induced by using a thin-wall modeling. In general, the coupling variation shown in Fig. 19 may be approximated as $1-0.45C_t$, which provides a clear estimation of the error induced in the present case when a thin-walled analysis is used.

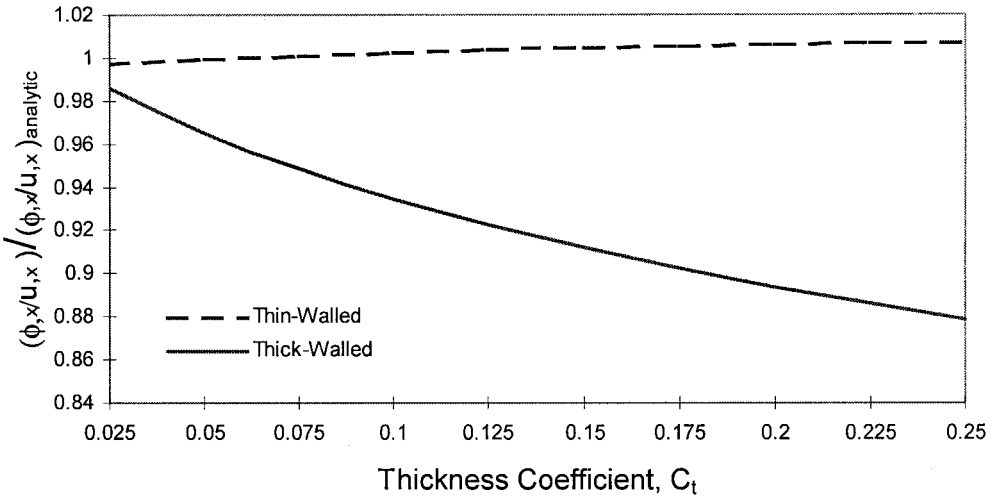

Fig. 13. The coupling magnitude of an antisymmetric composite box-beam due to a tip axial force normalized by the corresponding analytic thin-walled solution as a function of the thickness coefficient (uniform lamination angle of 15°, $a/b = 2$).

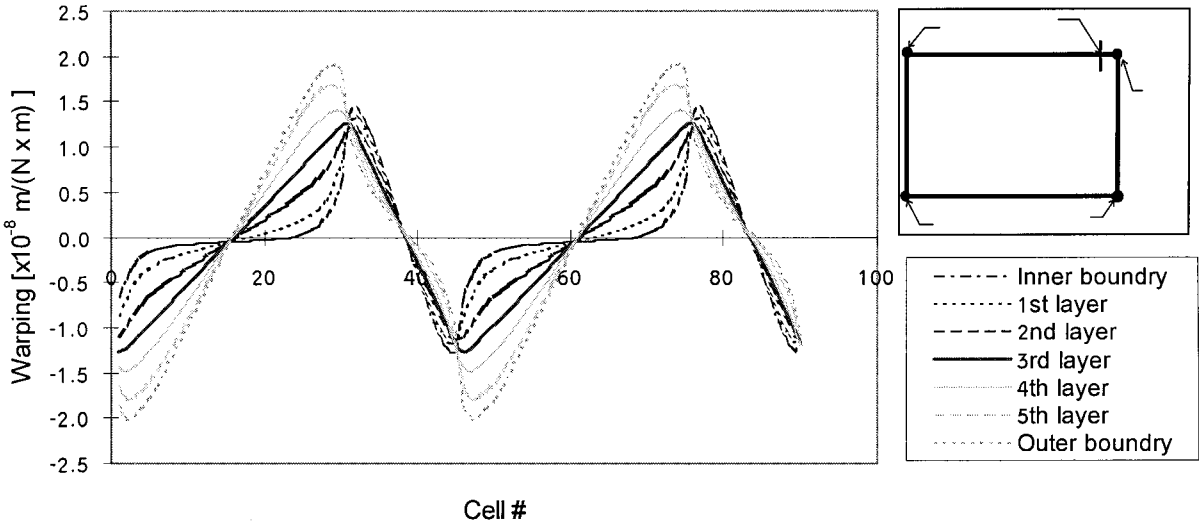

Fig. 14. The warping distribution as obtained by the thick-walled model for antisymmetric box-beam of $C_t = 0.168$ due to a tip torsional moment (uniform lamination angle of 15°, $a = 0.024$ m, $b = 0.012$ m, $t = 0.00076$ m).

The warping distribution for this case over the thickness middle line is presented in Fig. 20. In contrast with the case of an antisymmetric beam, this distribution is very interesting since its characteristics are changed along the beam. As shown, for the free end, the distribution is similar to the one obtained for isotropic beam due to a tip beamwise load, while in the inboard cross-sections, a

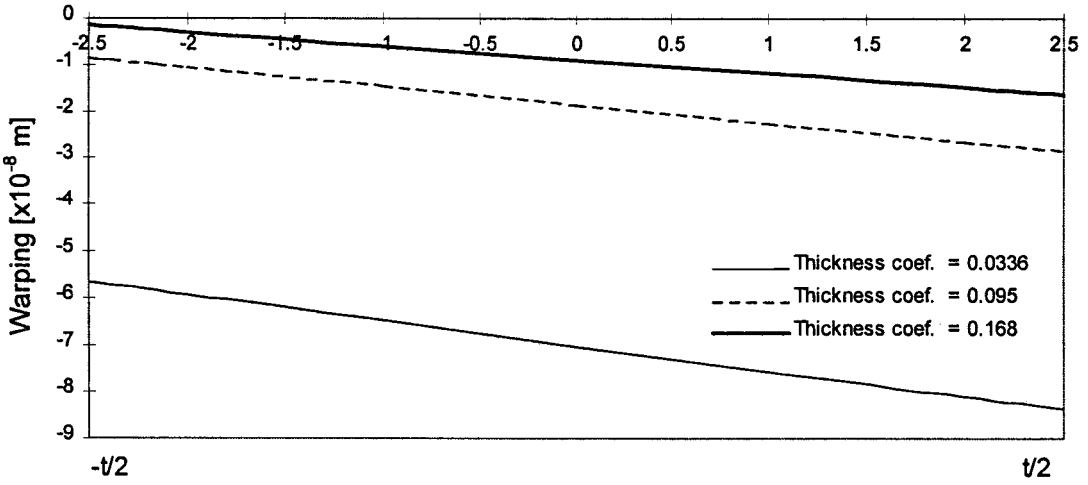

Fig. 15. The warping distribution over the wall thickness at $j = 6$ (see scheme in Fig. 14) as obtained by the thick-walled model for antisymmetric box-beams of various C_t values due to a tip torsional moment (uniform lamination angle of 15°, $a = 0.024$ m, $b = 0.012$ m, $t = 0.00076$ m, $M_x^{\text{tip}} = 1$ lb· ∈).

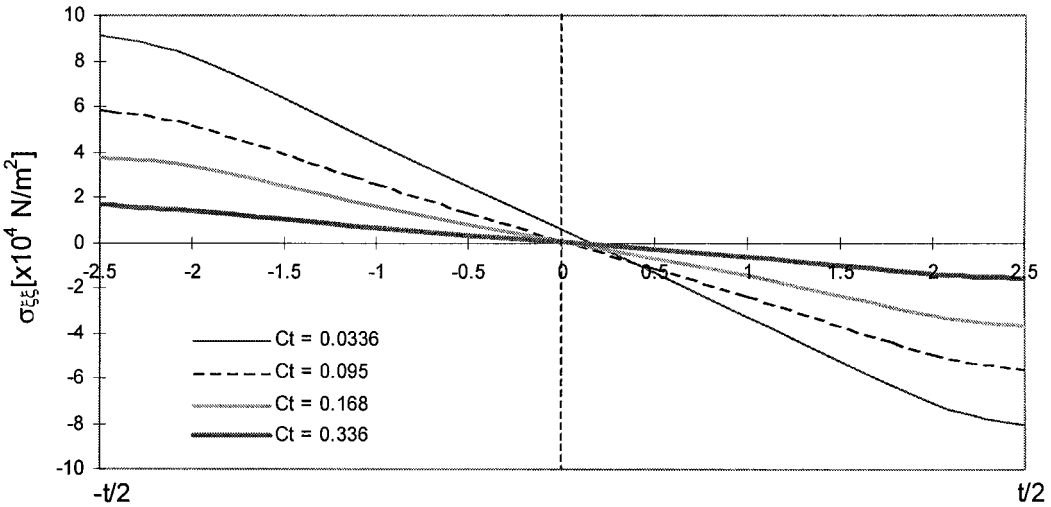

Fig. 16. The axial stress distribution over the wall thickness at $j = 6$ (see scheme in Fig. 14) as obtained by the thick-walled model for antisymmetric box-beams of various C_t values due to a tip torsional moment (uniform lamination angle of 15°, $a = 0.024$ m, $b = 0.012$ m, $t = 0.00076$ m, $M_x^{\text{tip}} = 1$ lb· ∈).

distribution which is similar to the one obtained for isotropic beam due to a tip torsional moment is superimposed on the one obtained at the tip. This may be explained by the fact that the twist $\phi_{,x}$, vanishes at the tip, but the value of $w_{,xxx}$ is constant along the beam since the shear force resultant is constant (due to the tip load).

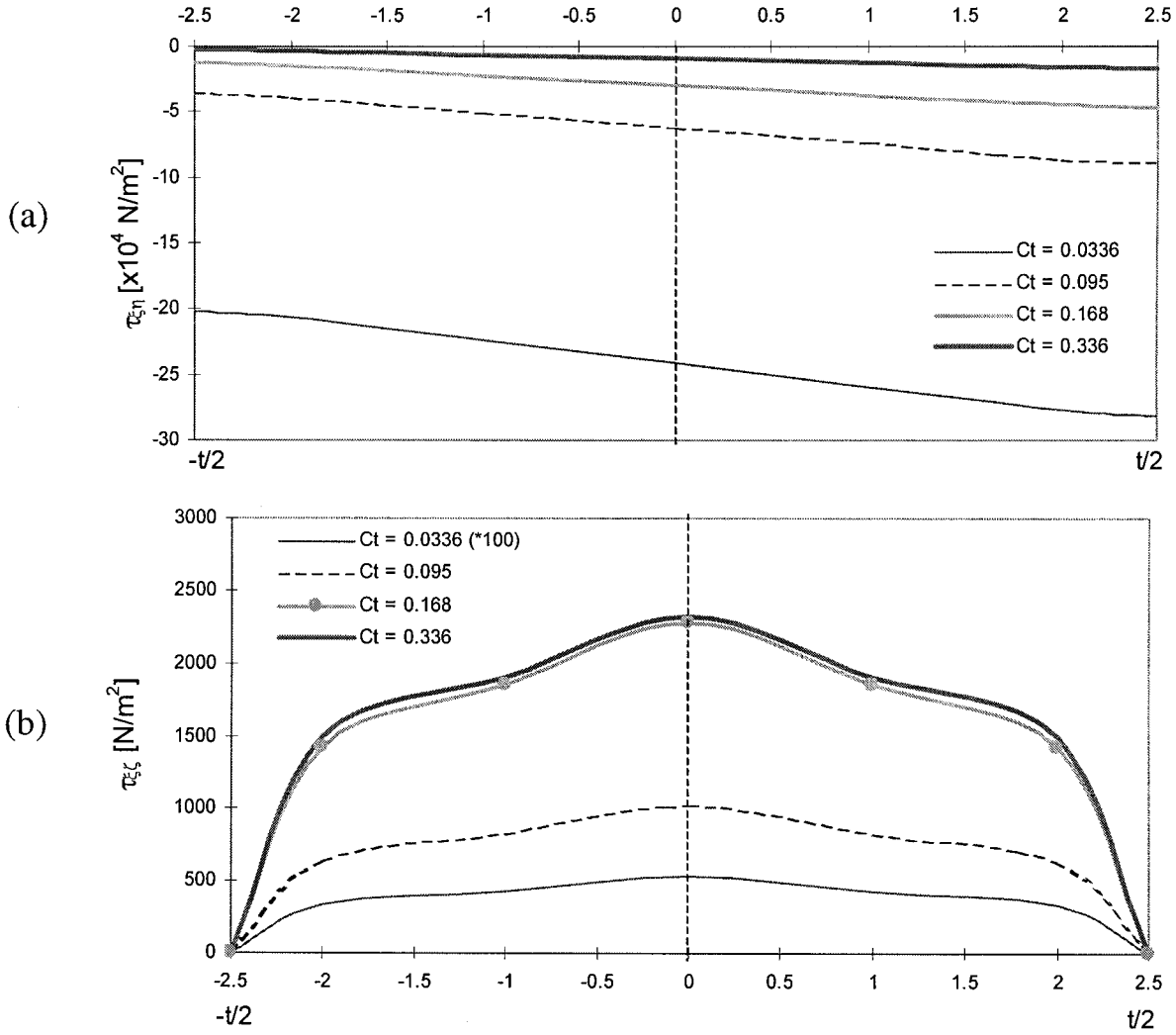

Fig. 17. The shear stresses distribution over the wall thickness at $j = 6$ (see scheme in Fig. 14) as obtained by the thick-walled model for antisymmetric box-beams of various C_t values due to a tip torsional moment (uniform lamination angle of 15°, $a = 0.024$ m, $b = 0.012$ m, $t = 0.00076$ m, $M_x^{\text{tip}} = 1$ lb· ∈): (a) The $\tau_{\xi\eta}$ component; (b) The $\tau_{\xi\zeta}$ component.

5. Concluding remarks

The influence of wall thickness on the structural behavior of composite blades has been studied using a finite-difference based numerical model. Unlike models for thin-walled beams, the shear stresses perpendicular to the wall thickness are accounted for. Due to the required warping modeling in the wall thickness direction, the numerical model for thick-walled cross-sections is by far more complicated and requires substantially larger computational resources. One of the aspects of the problem which is difficult to model is the connection between sharp corners of segments similar to the four corners in a box-beam.

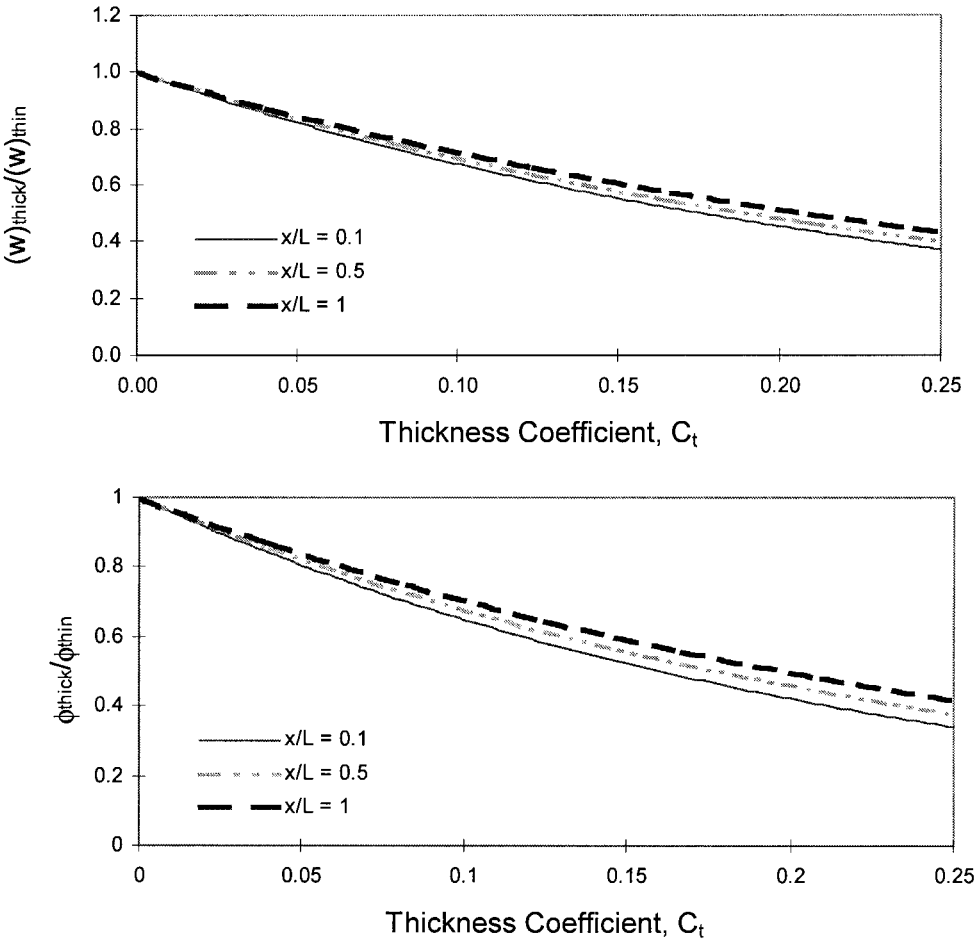

Fig. 18. The deformation due to a tip beamwise load of a symmetric composite box-beam as obtained by the thick-walled analysis normalized by the prediction of a thin-walled analysis for three spanwise locations (flange lamination angle of 10°, $a/b = 2$): (a) The beamwise displacement; (b) The twist angle.

The present model provides qualitative and quantitative indications regarding the amount of error induced by using thin-walled assumptions when dealing with thick-walled configurations. Approximate expressions for the above induced error are also provided. It has been shown that both the stiffness and the coupling magnitudes are considerably influenced by the wall thickness and the resulting discrepancy in the predicted characteristics may reach a value of 10–20% for thickness coefficient of $C_t \cong 0.2$.

Overall, it may be stated that basically, thick-walled composite beams maintain the composite induced coupling characteristics, while their magnitude is a function of the wall thickness. Typical changes in the stiffness and the composite induce couplings may be modeled as exponential functions in the form of e^{-aC_t} where a is in the range of $0.5 < a < 1.0$.

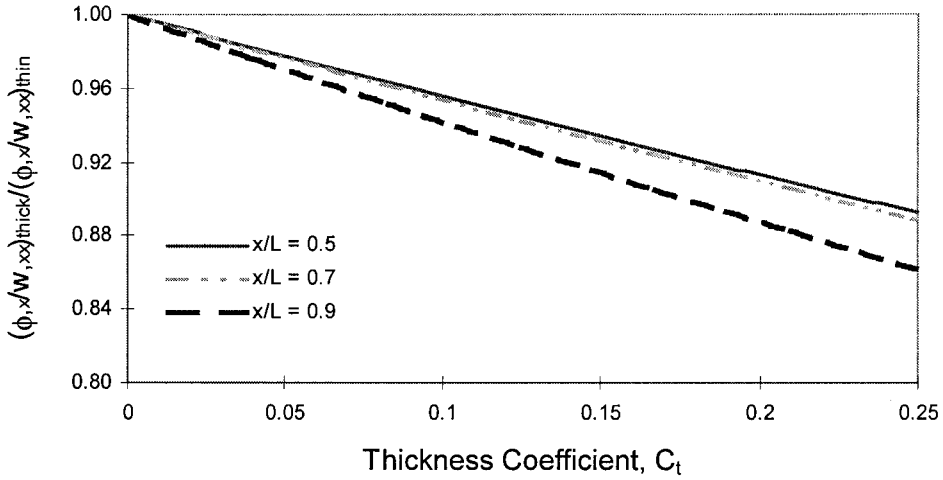

Fig. 19. The coupling magnitude due to a tip beamwise load of a symmetric composite box-beam as obtained by the thick-walled analysis normalized by the prediction of a thin-walled analysis for three spanwise locations (flange lamination angle of 10°, $a/b = 2$).

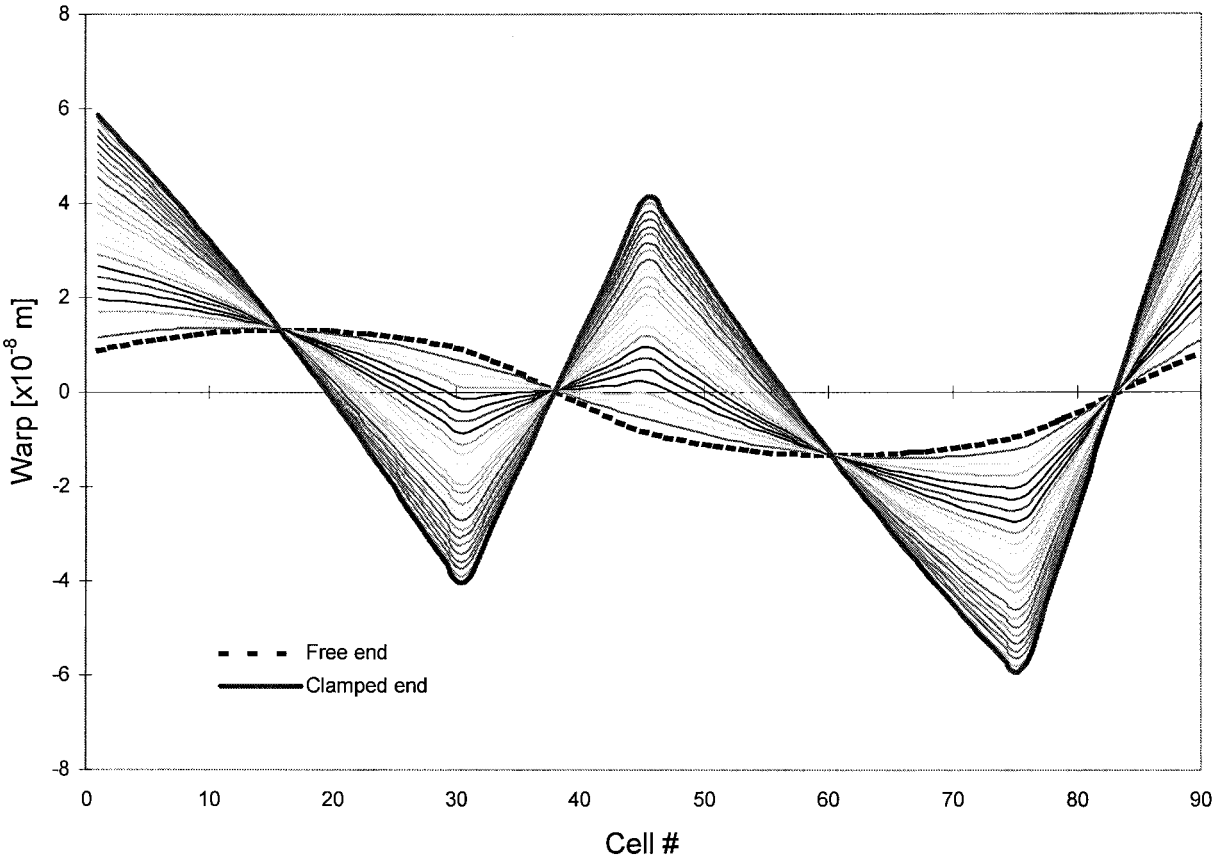

Fig. 20. The warping distribution over the thickness middle line due to a tip beamwise load of a symmetric composite box-beam for a range of spanwise locations (flange lamination angle of 10°, $a = 0.024$ m, $b = 0.012$ m, $t = 0.00076$ m, $F_x^{\text{tip}} = 1$ lb).

Appendix A. The elastic transformation matrix

The elastic transformation matrix $[D]$ (see Eq. (1)) is defined by a sequence of rotations of Euler angles (see also, Kalfon and Rand, 1993):

$$[D] = \begin{bmatrix} C_y C_z & S_x S_y C_z - C_x S_z & C_x S_y C_z + S_x S_z \\ C_y S_z & C_x C_z + S_x S_y S_z & -S_x C_z + C_x S_y S_z \\ -S_y & S_x C_y & C_x C_y \end{bmatrix}, \tag{A1}$$

where $C_i \equiv \cos(\theta_i)$, $S_i \equiv \sin(\theta_i)$ and $\theta_i = \theta_x, \theta_y, \theta_z$. Assuming that the rotations are executed by a rotation of θ_z about the Z axis, followed by a rotation of the resulting system by θ_y about its Y axis, followed by a rotation of the resulting system by θ_x about its X axis, the above rotation angles are given by:

$$\begin{aligned} &\theta_x = \phi, \quad \sin(\theta_y) = -\frac{w_{,X}}{L_2}, \quad \cos(\theta_y) = -\frac{L_1}{L_2}, \quad \sin(\theta_z) = \frac{v_{,X}}{L_1}, \quad \cos(\theta_z) = \frac{(1+u_{,X})}{L_1}, \\ &L_1 = \sqrt{(1+u_{,X})^2 + (v_{,X})^2} \quad L_2 = \sqrt{L_1^2 + (w_{,X})^2}. \end{aligned} \tag{A2}$$

In the linear case, $\theta_y \cong -w_{,X}$, $\theta_z \cong v_{,X}$, and $\cos(\theta_x)$, $\cos(\theta_y)$ and $\cos(\theta_z)$ may be treated as units. In addition, all derivatives with respect to X may be replaced with derivatives with respect to x. In this linear case, $[D]$ becomes:

$$[D] \cong \begin{bmatrix} 1 & -v_{,x} & -w_{,x} \\ v_{,x} & 1 & -\phi \\ w_{,x} & \phi & 1 \end{bmatrix}. \tag{A3}$$

References

Armanios, E.A., Badir, A.M., 1995. Free vibration analysis of anisotropic thin-walled close-section beams. AIAA Journal 33 (10), 1905–1910.

Bauchau, O.A., Chiang, W., 1993. Dynamic analysis of rotor flexbeams based on nonlinear anisotropic shell models. Journal of the American Helicopter Society 38 (1), 55–61.

Chandra, R., Chopra, I., 1991. Vibration characteristics of composite I-beam with elastic couplings under rotation. In: 47th Annual Forum of the American Helicopter Society, pp. 661–674 May 1991.

Chandra, R., Chopra, I., 1992a. Experimental–theoretical investigation of the vibration characteristics of rotating composite box beam. Journal of Aircraft 29 (4), 657–664.

Chandra, R., Chopra, I., 1992b. Structural behavior of two-cell composite rotor blades with elastic couplings. Journal of Aircraft 30 (12), 2914–2921.

Chandra, R., Stemple, A.D., Chopra, I., 1990. Thin-walled composite beams under bending, torsional, and extensional loads. Journal of Aircraft 27 (7), 619–625.

Epps, J.J., Chandra, R., 1996. The natural frequencies of rotating composite beams with tip sweep. Journal of the American Helicopter Society 41 (1), 29–36.

Kalfon, J.P., Rand, O., 1993. Nonlinear analysis of composite thin-walled helicopter blades. Journal of Computers and Structures 48 (1), 51–61.

Kim, T., Dugundji, J., 1991. Nonlinear large amplitude vibration of composite helicopter blade at large static deflection. In: 32nd AIAA/ASME/ASCE/AHS Structures, Structural Dynamics and Materials Conference, AIAA-91-1221-CP, pp. 2071–2081 April 8–12 1991.

Kim, T., Dugundji, J., 1993. Nonlinear large amplitude vibration of composite helicopter blade at large static deflection. AIAA Journal 31 (5), 938–946.

Kosmatka, J.B., Lake, R.C., 1996. Passive approach of controlling twist in composite tilt-rotor blades. In: SPIE Conference on Smart Structures and Integreted Systems, pp. 146–157 February 26–29 1996.

Librescu, L., Song, O., 1991. Behavior of thin-walled beams made of advanced composite materials and incorporating non-classical effects. Applied Mechanics Reviews 44 (11/2), s174–s180.

McCarthy, T.R., Chattopadhyay, A., 1996. A refined higher-order composite box-beam theory. In: 37th AIAA/ASME/ASCE/AHS Structures, Structural Dynamics and Materials Conference, AIAA Paper 96-1470 April 18–19 1996.

Ochoa, O.O., Reddy, J.N., 1992. Finite Element Analysis of Composite Laminates. Kluwer Academic Publisher Inc, The Netherlands.

Pai, P.F., Nayfeh, H.A., 1994. A fully nonlinear theory of curved and twisted composite rotor blades accounting for warping and three-dimensional stress effects. Int. J. Solid Structures 31 (9), 1309–1340.

Rand, O., 1994. Nonlinear analysis of orthotropic beams of solid cross-sections. Journal of Composite Structures 29 (1), 27–45.

Rand, O., 1998. Fundamental closed-form solutions for solid and thin-walled composite beams including a complete out-of-plane warping model. International Journal of Solid and Structures 35 (21), 2775–2793.

Rand, O., Barkai, S.M., 1996. Analytic insight into the structural couplings and nonlinear formulation of solid and thin-walled composite blades. In: 52nd Annual Forum of the American Helicopter Society June 4–6 1996.

Rapp, H., 1990. New computer codes for the structural analysis of composite helicopter structures. In: 16th European Rotorcraft Forum September 18–20.

Rappel, O., 1997. Investigation of the elastic couplings in thick-walled helicopter composite blades with large initial twist. Research Thesis, Technion–I.I.T., Haifa, Israel.

Song, O., Librescu, L., 1992. Free-vibration of composite rotating helicopter blades modelled as thin-walled beams. In: Proceedings of the American Society for Composites, pp. 636–649 October 13–15 1992.

Stemple, A.D., Lee, S.W., 1989. Large deflection static and dynamic finite element analysis of composite beams with arbitrary cross-sectional warping. In: 30th AIAA/ASME/ASCE/AHS Structures, Structural Dynamics and Materials Conference, AIAA Paper 89-1363-CP, pp. 1789–1798 April 1989.

Straub, F.K., Sangha, K.B., Panda, B., 1994. Advanced finite element modeling of rotor blade aeroelasticity. Journal of the American Helicopter Society 39 (2), 56–68.

Venkatesan, C., Friedman, P.P., Yuan, K., 1993. A new sensitivity analysis for structural optimization of composite rotor blades. In: 34th AIAA/ASME/ASCE/AHS Structures, Structural Dynamics and Materials Conference, AIAA-93-1644-CP, pp. 2952–2973.

Yuan, K., Friedmann, P.P., Venkatesan, C., 1992. Aeroelastic behavior of composite rotor blades with swept tips. In: 48th Annual Forum of the American Helicopter Society, pp. 1039–1059 June 3–5 1992.